JOURNAL OF PROPULSION AND POWER
Vol. 14, No. 1, January–February 1998

Reacting Flow Establishment in Ram Accelerators: A Numerical Study

S. Yungster,* K. Radhakrishnan,† and M. J. Rabinowitz‡
NASA Lewis Research Center, Cleveland, Ohio 44135

The temporal evolution of the combustion process that is established during projectile transition from the launch tube into the ram accelerator section containing an explosive hydrogen–oxygen–argon gas mixture is examined. The Navier–Stokes equations for chemically reacting flow are solved in a fully coupled manner, using an implicit, time-accurate algorithm. The solution procedure is based on a spatially second order, total variation diminishing scheme and a temporally second order, variable-step, backward differentiation formula method. The hydrogen–oxygen–argon chemistry is modeled with a nine-species, 19-step reaction mechanism. Results of the numerical simulations are presented for two representative cases. We study the temporal developments of shock-induced combustion and thrust force. Positive thrust occurs in both ram accelerator configurations presented; however, combustion in the boundary layer enhances its separation, ultimately resulting in unstart.

Introduction

THE ram accelerator is a chemical propulsion method for accelerating projectiles to very high speeds. In this device, developed at the University of Washington,[1–3] a projectile is accelerated inside a tube filled with an explosive gaseous mixture. The projectile can, in theory, be accelerated to velocities in excess of 10 km/s, while a high ballistic efficiency is maintained throughout the velocity range; several ram accelerator operation modes, spanning the 1–12 km/s velocity range have been proposed.[1–3] This concept can be scaled for projectile masses ranging from grams to hundreds of kilograms, and it has the potential for a number of applications, such as hypervelocity impact physics, hypersonic testing, and direct launch to orbit of acceleration-insensitive payloads.

The University of Washington ram accelerator consists of a light-gas gun or driver (using helium as the driver gas), launch tube, helium dump tank, ram accelerator section, final dump tank, and projectile decelerator section (Fig. 1). The gas gun delivers the initial acceleration to the projectile, which travels through the evacuated launch tube and enters the ram accelerator section. The large evacuated tank serves as a dump for the helium driver gas. The ram accelerator section can be divided into several parts, which may contain different explosive gas mixtures. These parts are separated from one another by thin Mylar diaphragms, which are ruptured by the projectile. In the high-speed mode of operation considered in this paper, ignition is achieved by means of shock heating. The resulting combustion reaction couples with the shock, forming either a shock-induced combustion wave or a detonation wave, depending on the mixture composition, pressure, and tube diameter. The final tank serves as a dump for the products of combustion.

Computational studies on the ram accelerator either have focused on steady-state solutions[4–9] or have been based on fully transient but inviscid approaches, utilizing simple one-step combustion models.[10–12] The first time-accurate, viscous simulation of the ram accelerator was reported by Nusca,[13] who used a global reaction mechanism for methane–air combustion.

A time-resolved flow calculation clearly provides a more realistic description of the combustion process in a ram accelerator than does a steady-state solution. Also, simple global reaction mechanisms are often inadequate for studying shock-induced combustion because the predicted induction times are incorrect.[5] Moreover, recent calculations[4,5,14] have demonstrated that viscous effects are of primary importance, not only in ram accelerators, but in any hypersonic propulsion concept. These findings illustrate the need for time-accurate, viscous (turbulent) computations using detailed (i.e., realistic) chemical reaction mechanisms.

Such calculations could not be accomplished, mainly because of the lack of an efficient numerical algorithm. Most previous time-accurate simulations of multispecies reacting flows used explicit or point-implicit methods, in which only the chemical source term is treated implicitly. The reason for not using the fully implicit methods that are commonly applied to nonreacting flows is partly because the governing equations are inherently stiff, thereby complicating the chemical source terms for these methods (for a general discussion of stiffness and how it arises, see Ref. 15). Because explicit or point-implicit methods are constrained by the Courant–Friedrichs–Lewy (CFL) condition, they are very inefficient for solving viscous, reacting flows. Consequently, new approaches have had to be adopted for simulating these flows.

Recently, we developed a computational fluid dynamics (CFD) code that addresses the need for efficient, time-accurate simulations of viscous, chemically reacting flows.[16] The solution procedure is based on a spatially second order, total variation diminishing (TVD) scheme, and a temporally second order, implicit, variable-step, backward differentiation formula (BDF) method. The inversion of large matrices is avoided by partitioning the system into reacting and nonreacting parts; a fully coupled interaction between the fluid flow and the combustion chemistry is, nonetheless, maintained by subiterating in time.

In the present paper we use this code to study the temporal evolution of the shock-induced combustion process in a ram accelerator, with an important objective being the assessment of the numerical method for such applications. We investigate projectile transition from the launch tube into the ram accel-

Received May 1, 1996; revision received Dec. 20, 1996; accepted for publication May 5, 1997.

*Institute for Computational Mechanics. Member AIAA.
†NYMA, Inc. Senior Member AIAA.
‡Internal Fluid Mechanics Division. Member AIAA.

Table 1 H_2–O_2–Ar reaction mechanism[a]

No.	Reaction	A	b	Θ
1	$H_2 + O_2 = HO_2 + H$	1.0×10^{14}	0.0	28197.38
2	$H + O_2 = OH + O$	2.6×10^{14}	0.0	8459.21
3	$H_2 + O = OH + H$	1.8×10^{10}	1.0	4481.37
4	$H_2 + OH = H + H_2O$	2.2×10^{13}	0.0	2593.15
5	$OH + OH = O + H_2O$	6.3×10^{12}	0.0	548.84
6[b]	$H + OH + M = H_2O + M$	2.2×10^{22}	−2.0	0.0
7[b]	$H + H + M = H_2 + M$	6.4×10^{17}	−1.0	0.0
8[b]	$H + O + M = OH + M$	6.0×10^{16}	−0.6	0.0
9[b]	$H + O_2 + M = HO_2 + M$	2.1×10^{15}	0.0	−503.52
10	$O + O + M = O_2 + M$	6.0×10^{13}	0.0	906.34
11	$HO_2 + H = OH + OH$	1.4×10^{14}	0.0	543.81
12	$HO_2 + H = H_2O + O$	1.0×10^{13}	0.0	543.81
13	$HO_2 + O = O_2 + OH$	1.5×10^{13}	0.0	478.35
14	$HO_2 + OH = H_2O + O_2$	8.0×10^{12}	0.0	0.0
15	$HO_2 + HO_2 = H_2O_2 + O_2$	2.0×10^{12}	0.0	0.0
16	$H + H_2O_2 = H_2 + HO_2$	1.4×10^{12}	0.0	1812.69
17	$O + H_2O_2 = OH + HO_2$	1.4×10^{13}	0.0	3222.56
18	$OH + H_2O_2 = H_2O + HO_2$	6.1×10^{12}	0.0	720.04
19[b]	$H_2O_2 + M = OH + OH + M$	1.2×10^{17}	0.0	22910.37

[a]Forward rate coefficient $k_f = AT^b \exp(-\Theta/T)$; units are moles, seconds, centimeters, and Kelvins.
[b]Third-body efficiencies: reaction 6, H_2O = 6.0; reaction 7, H_2O = 6.0; reaction 8, H_2O = 5.0; reaction 9, H_2O = 16.0, H_2 = 2.0; and reaction 19, H_2O = 15.0

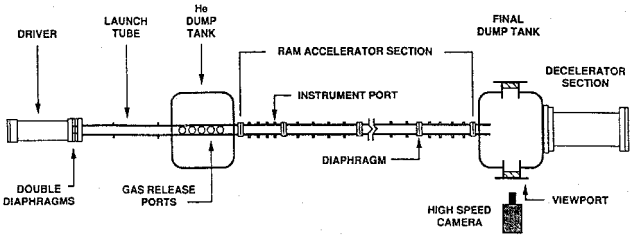

Fig. 1 Schematic of the University of Washington's ram accelerator facility.[3]

erator section containing an explosive hydrogen–oxygen–argon gas mixture. We also examine the effect of projectile shape on the resulting net thrust. The hydrogen–oxygen–argon chemistry is modeled with a nine-species, 19-step reaction mechanism (Table 1), which is based on the hydrogen–air mechanism developed by Jachimowski[17] for application to scramjet combustion.

Numerical Formulation

Governing Equations

The conservation form of the nonequilibrium Navier–Stokes equations describing two-dimensional or axisymmetric, chemically reacting flows involving N species can be written in general curvilinear coordinates (ξ, η), as follows:

$$\frac{\partial \boldsymbol{Q}}{\partial t} + \frac{\partial(\boldsymbol{F} - \boldsymbol{F}_v)}{\partial \xi} + \frac{\partial(\boldsymbol{G} - \boldsymbol{G}_v)}{\partial \eta} + \theta(\boldsymbol{S} - \boldsymbol{S}_v) = \boldsymbol{W} \quad (1)$$

where the parameter θ is zero for two-dimensional flow and it is one for axisymmetric flow, and $\boldsymbol{Q}$ is the $(N + 3)$th-dimensional column-vector of dependent variables:

$$\boldsymbol{Q} = J^{-1}(\rho_1, \rho_2, \ldots, \rho_N, \rho u, \rho v, e)^T \quad (2)$$

The dependent variables are the mass density ρ_i of the ith species ($i = 1, \ldots, N$), the total energy per unit volume e, and the momentum components per unit volume ρu and ρv, where ρ is the mixture mass density and u and v are the velocity components in the ξ and η directions. J is the grid Jacobian, and $\boldsymbol{F}$ and $\boldsymbol{G}$ are the inviscid flux vectors in the ξ and η directions, respectively. Similarly, $\boldsymbol{F}_v$ and $\boldsymbol{G}_v$ are the viscous fluxes. The terms $\boldsymbol{S}$ and $\boldsymbol{S}_v$ are axisymmetric source terms, and $\boldsymbol{W}$ is the chemical source term. A detailed description of the terms in Eq. (1) and additional state and constitutive equations needed for system closure are given by Yungster.[4]

Numerical Method

The numerical method used for solving Eq. (1) is summarized next; a detailed description is available elsewhere.[16] The equation set is discretized using a temporally second-order, variable-step, implicit, BDF method because its accuracy and efficiency for chemical kinetics applications have been well established.[19,20] The difference equations are solved step-by-step; that is, approximate solutions $\{\boldsymbol{Q}^n_{j,k}\}$, where the subscripts j and k denote spatial grid point indices in the ξ and η directions, are generated at the discrete time points t^n ($n = 1, 2, \ldots$). Thus, starting with the known initial conditions $\{\boldsymbol{Q}^0_{j,k}\}$ at time $t = t_0$, the numerical method advances the solution at each grid point in time, until the desired end state is reached. At each integration step, the time step Δt^n ($= t^{n+1} - t^n$) is selected automatically by using the procedure described by Yungster and Radhakrishnan.[16]

Assuming that approximate solutions have been produced at the discrete time points t^{n-j} ($j = 0, 1, \ldots$), the formula for advancing the solution to the current time t^{n+1} [i.e., for solving the governing equations over the time interval (t^n, t^{n+1})] can be written[16]

$$\begin{aligned}\Delta \boldsymbol{Q}^n_{j,k} = \gamma \Delta \boldsymbol{Q}^{n-1}_{j,k} - \beta \Delta t^n [&\tilde{\boldsymbol{F}}_{j+1/2,k} - \tilde{\boldsymbol{F}}_{j-1/2,k} + \tilde{\boldsymbol{G}}_{j,k+1/2} \\ &- \tilde{\boldsymbol{G}}_{j,k-1/2} - \tilde{\boldsymbol{F}}_{v_{j+1/2,k}} + \tilde{\boldsymbol{F}}_{v_{j-1/2,k}} - \tilde{\boldsymbol{G}}_{v_{j,k+1/2}} + \tilde{\boldsymbol{G}}_{v_{j,k-1/2}} \\ &- \boldsymbol{W}_{j,k} + \theta(\boldsymbol{S}_{j,k} - \boldsymbol{S}_{v_{j,k}})]^{n+1}\end{aligned} \quad (3)$$

where, for the current step

$$\Delta \boldsymbol{Q}^n_{j,k} = \boldsymbol{Q}^{n+1}_{j,k} - \boldsymbol{Q}^n_{j,k} \quad (4)$$

is the incremental solution vector, and γ and β are the variable-step BDF method coefficients. The terms $\tilde{\boldsymbol{F}}$ and $\tilde{\boldsymbol{G}}$ are the numerical fluxes in the ξ and η directions. They are computed using Yee's second-order TVD scheme.[21]

Equation (3) is linearized in a conservative manner and solved iteratively using a lower–upper relaxation procedure consisting of successive Gauss–Seidel (LU–SGS) sweeps. At each time step, successively improved approximate solutions to Eq. (3) are generated, until an appropriate convergence criterion is satisfied.[16]

For the method to remain temporally second order, the flux Jacobians ($\partial \boldsymbol{F}/\partial \boldsymbol{Q}$ and $\partial \boldsymbol{G}/\partial \boldsymbol{Q}$) must be exact; otherwise, the

accuracy reduces to first order. The inversion of large matrices is, however, avoided by partitioning the system into reacting and nonreacting parts; a fully coupled interaction between the flow and the combustion chemistry is, nevertheless, preserved by subiterating in time. The benefit of the partitioning is that the computational cost of the linear algebra associated with matrix formation and LU decomposition is the same as that of the commonly used point-implicit methods. The reason is that the matrices arising in the two approaches are the same size.

Another important advantage of our method is that it remains stable for large values of the CFL number, so that large time steps can be used, thereby minimizing execution time.

Results

The goal of the present work was to study numerically the establishment of reacting flow during projectile entrance into the ram accelerator section, to improve our understanding of the physical and chemical processes in ram accelerators. Because time-accurate, viscous, chemically reacting flow simulations of ram accelerators using detailed reaction mechanisms have not previously been attempted, it is important to demonstrate the efficacy of our numerical method for this application before attempting parametric studies. The accuracy of our method has previously been demonstrated for steady-state flows, inviscid and viscous and nonreacting and reacting, by numerous studies, including shock-boundary interactions[4] and oblique and normal shock-induced combustion and detonation.[5,22,23] Recently, the solution method was extended to enable simulation of time-dependent phenomena.[16] To validate the time-accurate portion, we studied unsteady shock reflection from a wedge[14] and several pulsating shock-induced combustion flows,[16] one of which, because of its relevance to ram accelerator phenomena, is discussed in this paper. In addition, to examine further the time-accurate feature of our code, a shock-wave diffraction simulation, for which results of previous numerical studies are available, is presented. Although these benchmark cases involve inviscid flow, the viscous part of the algorithm has been validated in earlier studies.[4,5,22,23] Before discussing these benchmark cases, however, we first present results that establish that the spatial differencing method used in our algorithm is second-order accurate.

Spatial Accuracy

To verify the second-order spatial accuracy of our algorithm, we examined supersonic nonreacting flow in a nozzle by solving the two-dimensional Euler equations. The uniform inflow condition, $M = 2.5$, was specified at the inflow plane, and zero-order extrapolation was used at the outflow boundary. Because there is no analytical solution for this two-dimensional problem, we adopted a commonly used procedure. Numerical solutions were generated with progressively finer grids until the solution showed essentially no change with further grid refinement, that is, the solution had become grid independent. The numerical solution obtained with the finest grid used (800 grid points) was defined to be the standard solution and was used to estimate global errors in the solutions generated with the coarser grids.

The geometry and computed steady-state density contours obtained with the finest grid (i.e., standard solution for density) are shown in Fig. 2a. Interactions between compression and expansion waves give rise to an oscillatory density distribution that would be difficult to capture accurately with a first-order scheme. As a further check of our standard solution, it was compared with results produced by the widely used NPARC code,[24] using the same fine grid discussed in the preceding text. The density distributions obtained along the symmetry plane with the two codes are shown in Fig. 2b. Excellent agreement can be observed between the results produced by the two methods.

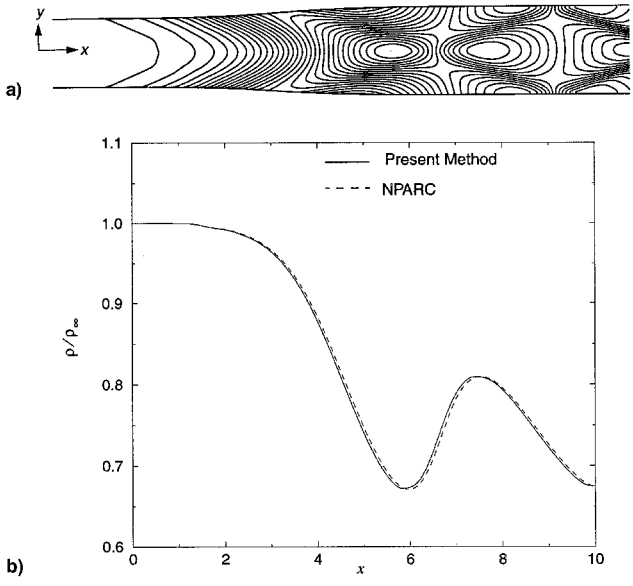

Fig. 2 Computed flow ($M = 2$) in a two-dimensional nozzle whose shape is described by $y = \sqrt{\{1.398 + 0.347 \times \tanh[0.8(x - 4)]\}}/\pi$: a) density contours and b) normalized density distributions along nozzle centerline.

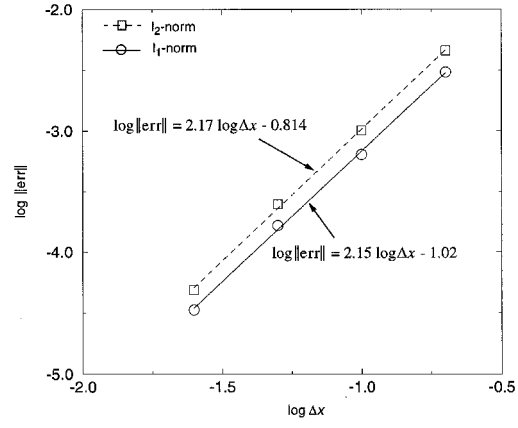

Fig. 3 Error norms vs axial grid spacing (Δx) for nozzle flow given in Fig. 2.

For the solutions obtained with the coarser grids (50, 100, 200, and 400 points, respectively), the l_1 and l_2 norms of the error, $\|\text{err}\|_1$ and $\|\text{err}\|_2$, respectively, were computed as follows:

$$\|\text{err}\|_1 = \frac{1}{N}\sum_{i=1}^{N} |\rho_i - \rho_{ST,i}|$$

$$\|\text{err}\|_2 = \left[\frac{1}{N}\sum_{i=1}^{N} (\rho_i - \rho_{ST,i})^2\right]^{1/2} \tag{5}$$

Here, N is the total number of grid points in the coarsest grid examined (i.e., $N = 50$), ρ_i is the density at grid point i of the coarsest grid, and $\rho_{ST,i}$ is the standard solution value for density at grid point i. Figure 3 shows the variation of the l_1 and l_2 norms of the local error with axial grid spacing, along with least-squares straight line fits to the numerical results. It is clear from this figure that the method is second-order accurate.

Benchmark Test Cases

The first test case, taken from the work of Young and Yee,[25] simulates shock wave diffraction from a 40-deg wedge in air, as shown in Fig. 4a. The top of the wedge was rounded, with a radius of curvature of 0.17 times the base width. Figures

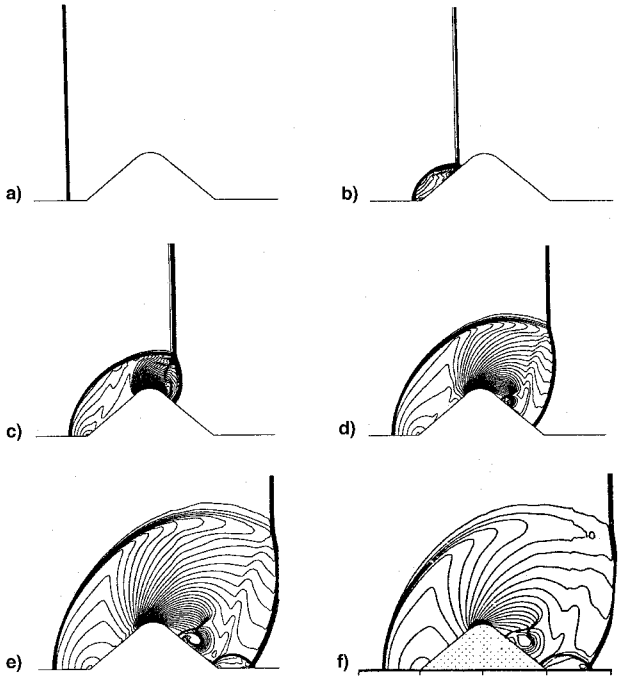

Fig. 4 Computed density contours: a)–e) temporal evolution of shock diffraction by wedge using present method, and f) results of Young and Yee[24] at approximately the same instant as that of Fig. 4e.

4b–4f present the temporal evolution of the airflow during the nonreacting diffraction process for an incident shock Mach number M_s of 2.0. A 313 × 140 uniform grid was used, and inviscid flow was assumed.[25] This test problem is well suited for evaluating the time-accurate procedure used in our numerical method because viscous and chemistry effects are not involved, but a time-dependent flow is considered; therefore, the only feature of our method that is tested is the time-accurate procedure.

Figure 4b shows density contours during the formation of the triple point, with the Mach stem and a contact discontinuity emanating from it. As the shock wave moves over the rounded top, the Mach stem evolves into a curved shock (Figs. 4c and 4d), which travels slightly faster than the incident shock. Figure 4e shows the reflection of the shock from the flat rear portion of the body and the formation of a new Mach stem. Figure 4f shows the computational results obtained by Young and Yee[25] at approximately the same instant as that of Fig. 4e. Their calculations were based on the MacCormack symmetric TVD method.[26] The agreement between the two sets of results is excellent. (Although not discussed here, the two sets of results displayed similar levels of agreement at previous times).

The second test case was a simulation of Lehr's[27] ballistic range experiments, which consisted of 15-mm spherically nosed projectiles being fired into a premixed, stoichiometric hydrogen–air mixture. Figure 5a shows the shadowgraph image obtained by Lehr[27] for a Mach number M = 4.18. For this case, the computational results[16] are shown in Fig. 5b in the form of density contours. They were obtained using a 220 × 220 uniform grid and a nine-species, 19-step reaction mechanism for the hydrogen–oxygen chemistry (Table 1). Under the conditions of the test, the reacting flow was unstable, resulting in a higly regular, periodic flow structure. Figures 5a and 5b show that the numerical simulation has captured all of the essential features of the flow; that is, a bow shock, a detached combustion front near the projectile surface, a single pulse in the combustion front at the nose region, and a contact discontinuity emanating from this pulse. Although these comparisons are qualitative in nature, quantitative comparisons between theoretical results and experimental measurements were accomplished by means of the frequency of oscillation. For the conditions shown in Figs. 5a and 5b, Lehr[27] obtained a frequency of oscillation of 148 kHz; the computed frequency was 163 kHz, which compares favorably with the results (160 Hz) of Matsuo et al.[28] Our computations for other flow conditions exhibited even better agreement with experimental data.[16] It must be emphasized that to compute the oscillation frequency accurately, the numerical method must be able to accurately compute ignition delay times, as well as shock waves, expansion waves, contact discontinuities, reaction fronts, and their interactions with one another.[16]

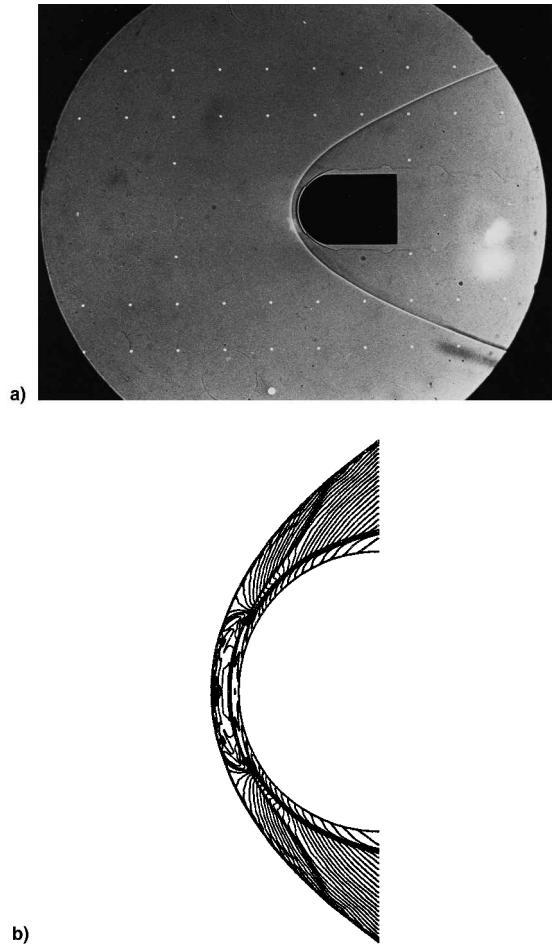

Fig. 5 Experimental and computational results for projectile moving at M = 4.18 in stoichiometric hydrogen–air mixture: a) experimental shadowgraph image[26] and b) computed density contours.[16]

Ram Accelerator Reacting Flow Establishment

Three simplifying assumptions were made in this work, which represents a preliminary numerical study of reacting flow establishment in a ram accelerator, with the goals of both assessing the efficacy of the numerical method for such applications and gaining insight into ram accelerator operation. First, the bursting of the diaphragm between the buffer section and the ram accelerator section occurred instantaneously and ideally, at the moment of projectile arrival. Second, to avoid computations involving extremely large pressure gradients between the evacuated launch tube and the first ram accelerator section, a buffer section containing oxygen was introduced between the two segments (Fig. 6). Third, an isothermal boundary condition was imposed at the projectile surface.

We also examined the effects of an adiabatic boundary condition. The result was very rapid combustion all along the boundary layer, with unstart following immediately thereafter. In addition, the calculated temperature at the projectile surface was so high that overheating and ultimate destruction (melting/burning) of the projectile was certain to occur. These results

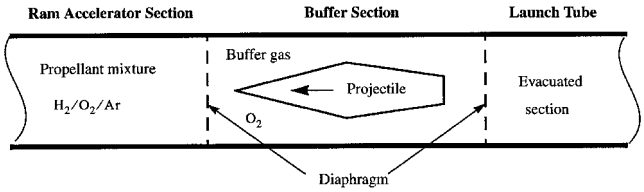

Fig. 6 Ram accelerator configuration considered in the present study.

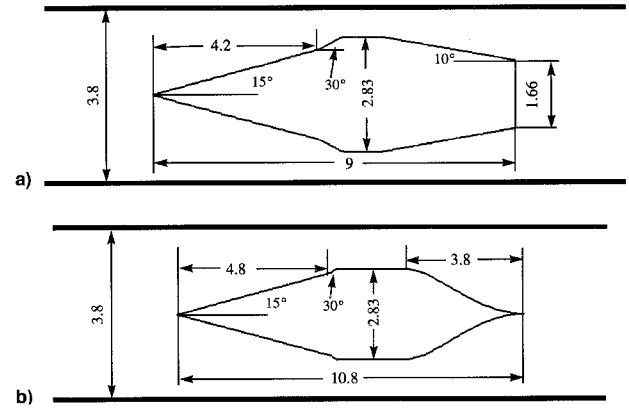

Fig. 7 Schematic of ram accelerator projectiles used in this study. Dimensions are in centimeters.

suggest the necessity of providing some form of projectile cooling. For example, hollow projectiles can be filled with a cold gas or even liquid nitrogen to provide the necessary cooling.

Various projectile configurations, flow conditions, and hydrogen–oxygen–argon mixtures were studied; we present two of these cases to represent our findings. In the first case (Fig. 7a), the tail was truncated to closely resemble the projectiles used in the University of Washington experiments.[1–3] In the second case (Fig. 7b), the tail ended at a sharp point, and the projectile shape was modified with the aim of maximizing thrust. Both cases modeled the transition from a pure oxygen buffer section at p = 1 atm and T = 300 K into a ram accelerator section containing an explosive hydrogen–oxygen–argon mixture at the same pressure and temperature. To illustrate both robustness of our numerical method and effects of flow parameters, the flow was assumed to be laminar in the first case and turbulent in the second.

Accelerating frame of reference effects were neglected in this study, based on the rigorous analysis of Bruckner et al.[2] Their study showed that the projectile acceleration terms in the governing equations can be neglected for accelerations less than approximately 30,000–40,000 g. This acceleration level is higher than that experienced by current ram accelerator projectiles (≈15,000 g). Assuming an acceleration of 20,000 g, the projectile would have increased its velocity by approximately 20 m/s during a time interval of 100 μs, which, for reasons discussed later, was approximately the duration of our simulation. Because this velocity increase represents less than 1% of the projectile's speed (>2 km/s), its acceleration was ignored in the present calculations.

Case 1

This case considered the ram accelerator configuration shown in Fig. 7a. The explosive gas mixture in the ram accelerator section was $H_2 + 3.5O_2 + 1.5Ar$. The projectile's speed was 2136.5 m/s, which corresponded to Mach numbers of 6.5 in the buffer section and 6.065 in the ram accelerator section. The flow was assumed to be laminar, and a constant wall temperature of 300 K was specified at the projectile surface. A two-block 210 × 110, 80 × 159 nonuniform grid was

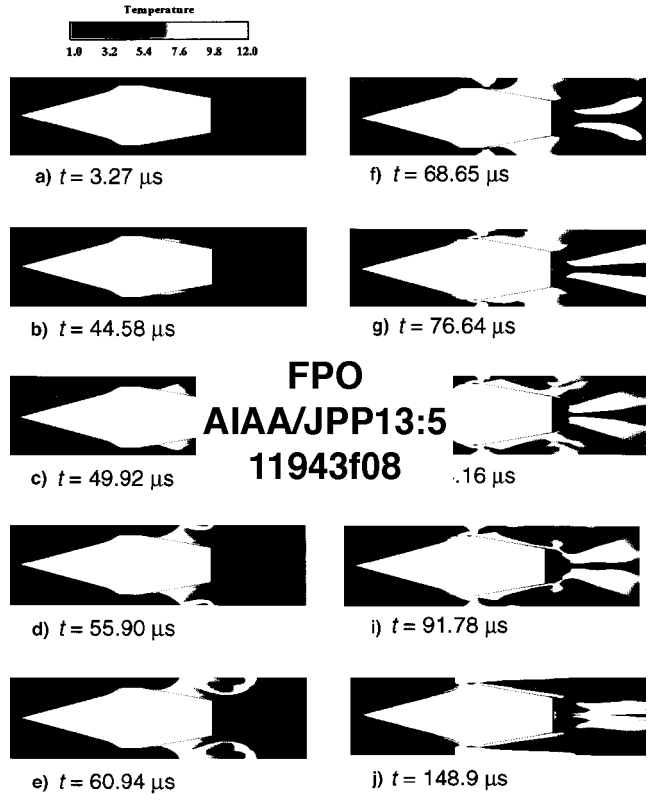

Fig. 8 Nondimensional temperature contours showing reacting flow establishment in ram accelerator for case 1. Projectile speed = 2136.5 m/s; reacting mixture: $H_2 + 3.5O_2 + 1.5Ar$; T_∞ = 300 K.

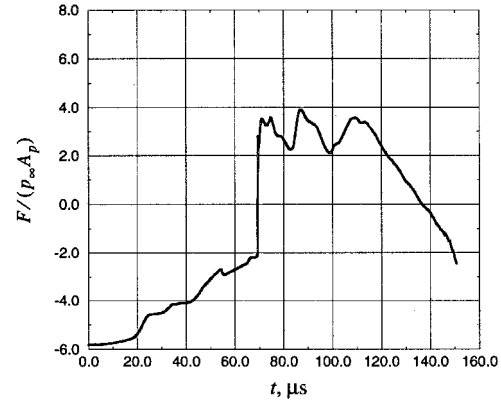

Fig. 9 Nondimensional net thrust force on ram accelerator projectile. (A_p is the maximum cross-sectional area of the projectile.)

utilized, based on previous grid-independence studies for similar ram accelerator configurations.[4]

The time evolution of the flowfield is shown in Fig. 8 in the form of nondimensional temperature T/T_∞ contours, where T_∞, the freestream temperature, was 300 K. Figure 8a shows the projectile just before entering the ram accelerator section. The reflected shock wave from the tube creates a small separation of the boundary layer, which grows slowly with time. At t = 44.58 μs, ignition occurs in the projectile boundary layer (Fig. 8b). Combustion spreads both downstream and toward the ram accelerator tube (Fig. 8c). A shock-induced combustion wave is established and then reflected from the tube wall (Figs. 8d and 8e). The shock-induced combustion wave produces a large pressure over the back of the projectile, and positive thrust begins to be generated at t = 69.4 μs (Fig. 9). At t = 68.65 μs, the reflected conical shock created by the small ramp ignites the mixture, creating a new shock-induced combustion wave (Fig. 8f). This wave magnifies the separation in the pro-

jectile's boundary layer, and combustion spreads upstream through the boundary layer, as shown in Figs. 8g–8i, ultimately resulting in unstart at $t = 135$ μs (Fig. 8j).

The temporal variation of the net thrust on the projectile is shown in Fig. 9. During transition into the ram accelerator section, the drag decreases, because the Mach number of the flow ahead of the projectile abruptly drops from 6.5 to 6.065. Therefore, as the projectile penetrates into the ram accelerator section, the wave drag decreases progressively. Positive thrust is produced after the first shock-induced combustion wave hits the projectile (at $t = 69.4$ μs). A new peak is formed after the second shock-induced combustion wave hits the projectile (at $t = 82$ μs). As the combustion front moves upstream, a third peak forms (at $t = 110$ μs), after which the combustion front moves toward the projectile nose, resulting in reduced thrust and ultimately unstart. These results reinforce our previous findings on the importance of viscous effects on ram accelerator performance, and, hence, the need for both including the viscous terms in the governing equations and the accurate modeling of these terms.[4,5]

This simulation required 4900 iterations and 15.2 h of CPU time on a Cray C90 computer; the maximum CFL number varied between 3–11.

Case 2

The ram accelerator configuration shown in Fig. 7b was considered. The 30-deg ramp was shortened, and the projectile's shape modified with the aim of improving performance. The explosive gas mixture in the ram accelerator section was $H_2 + 3.75O_2 + 0.25Ar$. The projectile's velocity was 2136.5 m/s, corresponding to Mach numbers of 6.5 in the buffer section and 5.863 in the ram accelerator section. The flow was assumed to be turbulent, and a constant wall temperature of 300 K was specified at the projectile surface. For this calculation a turbulent boundary layer was assumed and the Baldwin–Lomax turbulence model[29] was used, because it is simple and gives reasonable results across a wide range of Mach numbers, from subsonic to hypersonic.[30] A 315 × 110 nonuniform grid was utilized, again based on our previous experience with similar types of ram accelerator configurations.

The temporal evolution of the flowfield is shown in Fig. 10 in the form of nondimensional temperature T/T_∞ contours, where $T_\infty = 300$ K. Figure 10a shows the projectile just before bursting of the diaphragm. The initial flow development is similar to that described for the preceding case. That is, ignition begins in the projectile's boundary layer (Fig. 10b), and a shock-induced combustion wave is established (Fig. 10c). This wave is then reflected from the ram accelerator tube (Fig. 10d), and when it reaches the projectile surface, a large pressure is established over the back of the projectile (Fig. 10e), producing positive thrust at $t = 58.9$ μs (Fig. 11).

For this ram accelerator configuration, the reflected shock created by the ramp is not strong enough to ignite the mixture. In Fig. 10g, combustion is seen to propagate upstream through the boundary layer. The combustion occurring inside the small separation bubble forces it to expand. The boundary-layer combustion continues to propagate upstream (Fig. 10h), ultimately resulting in unstart of the ram accelerator (Fig. 10i). Thus, even when the boundary layer is turbulent, unstart occurs by the same mechanism as in the laminar case.

The net thrust on the projectile is plotted in Fig. 11. The initial development of the thrust force is similar to that for the previous case. That is, the drag decreases progressively as the projectile enters the ram accelerator section, where the speed of sound is higher (and the Mach number is therefore lower). There is then a sudden jump to positive thrust (at $t = 58.9$ μs), when the reflected shock-induced combustion wave reaches the projectile surface. The thrust shows a short increase (at $t = 78$ μs) prior to unstart (at $t = 89$ μs).

This simulation required 3400 iterations and 7.8 h of CPU time on a Cray C90 computer, with a maximum CFL number of between 4–10.

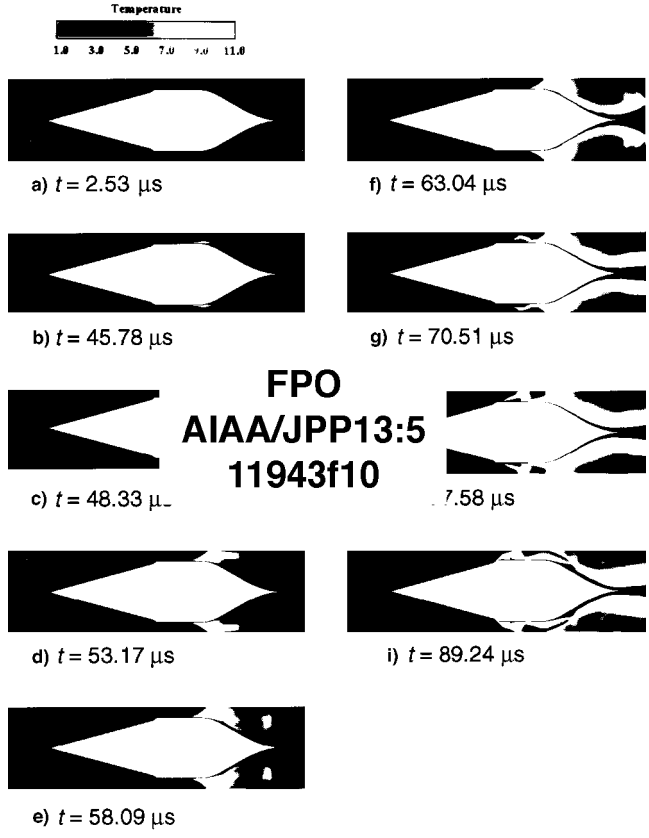

Fig. 10 Nondimensional temperature contours showing reacting flow establishment in ram accelerator for case 2. Projectile speed = 2136.5 m/s; reacting mixture: $H_2 + 3.75O_2 + 0.25Ar$; $T_\infty = 300$ K.

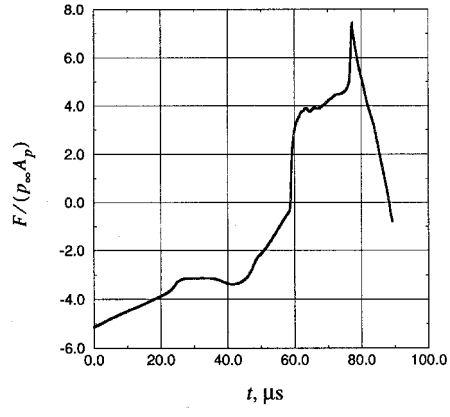

Fig. 11 Nondimensional net thrust force on ram accelerator projectile. (A_p is the maximum cross-sectional area of the projectile.)

Pressure Distribution

Figures 12 and 13 show the pressure distribution on the projectile at various times for the two cases previously described. The results for case 1 are separated into surface pressure distribution (Fig. 12a) and projectile base pressure distribution (Fig. 12b). At $t = 49.92$ μs, the surface pressure is similar to that observed just before diaphragm bursting ($t = 3.27$ μs), except that the pressure level at the nose is smaller because of the transition to a lower Mach number flow. At $t = 76.64$ μs and $t = 91.78$ μs, the high pressure established over the back of the projectile, caused by the shock-induced combustion wave, can be clearly seen. The pressure plots at these times show four peaks. The two small peaks are both caused by boundary-layer separation. The first of the larger two peaks is produced by the ramp, and the second peak is

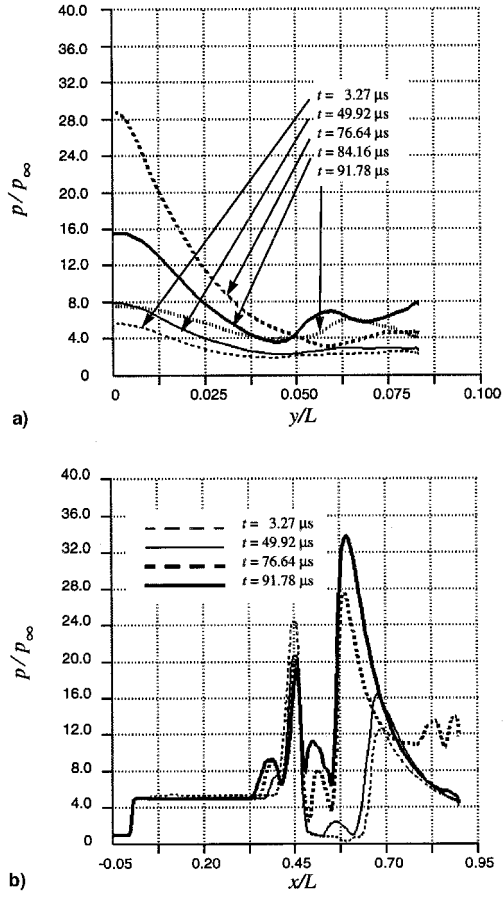

Fig. 12 Nondimensional pressure distribution for case 1 at various times: a) projectile surface and b) projectile base. Note: horizontal distance x is measured from the nose tip, vertical distance y is measured from symmetry axis, and L (=10 cm) is a length scale.

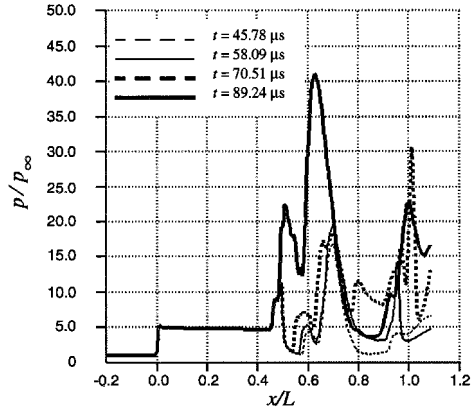

Fig. 13 Nondimensional pressure distribution along the projectile surface for case 2 at various times. Note: horizontal distance x is measured from the nose tip and L (=10 cm) is a length scale.

produced by the shock-induced combustion wave. The pressure distribution on the projectile base is presented in Fig. 12b. The base pressure increases significantly during the transient phase, and then decreases to a level somewhat higher than that prior to combustion.

The pressure distribution for the second case is given in Fig. 13. The plots at t = 45.78 and 58.09 μs give the distribution after ignition, but before positive thrust is being produced. At t = 70.51 μs, positive thrust is being created, and the high pressure over the back of the projectile is evident in Fig. 13. After unstart (t = 89.24 μs), a large pressure is established over the ramp, resulting in a small, but negative, total thrust at this time.

The unstart observed in both cases suggests the need to exert some control of the boundary-layer flow, for example, through the use of boundary-layer bleed or, as proposed in Ref. 12, a pure hydrogen core maintained inside a thin-walled balloon. The latter method would not only prevent boundary-layer combustion, but would reduce the gasdynamic heating of the projectile.

Conclusions

A numerical investigation of the temporal evolution of the reacting flowfield established during projectile transition from the launch tube into the ram accelerator section was presented. A methodology for simulating the reacting flow establishment was described, and computations for two configurations were presented, to illustrate the capability of the numerical approach. The efficiency of the time-accurate, fully implicit method was demonstrated by computing high-speed, reacting, viscous flows at CFL numbers as high as 11.

Calculations with adiabatic projectiles showed very rapid combustion all along the boundary layer, resulting in very high projectile surface temperatures and inducing unstart immediately after ignition. These results suggest the necessity of cooling the projectile. Even when the projectile surface was cooled and its temperature maintained at 300 K, ignition was obtained in the boundary layer for all projectile geometries and hydrogen–oxygen–argon mixtures considered. The combustion in the boundary layer spread downstream and toward the ram accelerator tube, establishing a shock-induced combustion wave. Subsequently, combustion also propagated upstream through the separated boundary layer. This process unstarted the ram accelerator, suggesting the need to exert control of the boundary layer.

Acknowledgments

The authors thank H. F. Lehr of the French–German Research Institute Saint-Louis for providing them with original photographs of his experimental results.

References

[1]Hertzberg, A., Bruckner, A. P., and Bogdanoff, D. W., "Ram Accelerator: A New Chemical Method for Accelerating Projectiles to Ultrahigh Velocities," *AIAA Journal*, Vol. 26, No. 2, 1988, pp. 195–203.

[2]Bruckner, A. P., Knowlen, C., Hertzberg, A., and Bogdanoff, D. W., "Operational Characteristics of the Thermally Choked Ram Accelerator," *Journal of Propulsion and Power*, Vol. 7, No. 5, 1991, pp. 828–836.

[3]Hertzberg, A., Bruckner, A. P., and Knowlen, C., "Experimental Investigation of Ram Accelerator Propulsion Modes," *Shock Waves*, Vol. 1, No. 1, 1991, pp. 17–25.

[4]Yungster, S., "Numerical Study of Shock-Wave Boundary Layer Interactions in Premixed Combustible Gases," *AIAA Journal*, Vol. 30, No. 10, 1992, pp. 2379–2387.

[5]Yungster, S., and Rabinowitz, M. J., "Computation of Shock-Induced Combustion Using a Detailed Methane-Air Mechanism," *Journal of Propulsion and Power*, Vol. 10, No. 5, 1994, pp. 609–617.

[6]Chew, G., and Bruckner, A. P., "A Computational Study of Projectile Nose Heating in the Ram Accelerator," AIAA Paper 94-2964, June 1994.

[7]Soetrisno, M., and Imlay, S. T., "Simulation of the Flow Field of a Ram Accelerator," AIAA Paper 91-1915, June 1991.

[8]Weirs, V. G., and Candler, G. V., "Ram Accelerator Simulations Using Elemental Conservation Equations," AIAA Paper 94-2966, June 1994.

[9]Nusca, M. J., "Numerical Simulation of Fluid Dynamics with Finite-Rate and Equilibrium Combustion Kinetics for the 120-mm Ram accelerator," AIAA Paper 93-2182, June 1993.

[10]Li, C., Kailasanath, K., Oran, E. S., Boris, J. P., and Landsberg, A. M., "Numerical Simulations of Transient Flows in Ram Accelerators," AIAA Paper 93-1916, June 1993.

[11]Thibault, P. A., Penrose, J. D., and Sulmistras, A., "Studies on Detonation Driven Hollow Projectiles," *Combustion in High-Speed*

Flows, edited by J. Buckmaster et al., Kluwer Academic, Norwell, MA, 1994, pp. 421–443.

[12]Cambier, J., and Bogdanoff, D. W., "Ram Acceleration from a Two-Phase Detonative System," *Proceedings of the 1st International Ram Accelerator Workshop* (Saint-Louis, France), 1993.

[13]Nusca, M. J., "Reacting Flow Simulation for a Large Scale Ram Accelerator," AIAA Paper 94-2963, June 1994.

[14]Yungster, S., and Radhakrishnan, K., "Computational Study of Flow Establishment in Hypersonic Pulse Facilities," *Proceedings of the 2nd International Workshop on Ram Accelerators*, Univ. of Washington, Seattle, WA, 1995; also NASA CR-198407, 1995; also *Shock Waves* (to be published).

[15]Shampine, L. F., and Gear, C. W., "A User's View of Solving Stiff Ordinary Differential Equations," *Society for Industrial and Applied Mathematics Review*, Vol. 21, 1979, pp. 1–17.

[16]Yungster, S., and Radhakrishnan, K., "A Fully Implicit Time Accurate Method for Hypersonic Combustion: Application to Shock-Induced Combustion Instability," NASA TM-106707; also AIAA Paper 94-2965; also *Shock Waves*, Vol. 5, 1996, pp. 293–303.

[17]Jachimowski, C. J., "An Analytical Study of the Hydrogen-Air Reaction Mechanism with Application to Scramjet Combustion," NASA TP-2791, Feb. 1988.

[18]Radhakrishnan, K., and Hindmarsh, A. C., "Description and Use of LSODE, the Livermore Solver for Ordinary Differential Equations," NASA RP-1327, Dec. 1993.

[19]Radhakrishnan, K., "Combustion Kinetics and Sensitivity Analysis Computations," *Numerical Approaches to Combustion*, edited by E. S. Oran and J. P. Boris, AIAA, Washington, DC, 1991, pp. 83–128.

[20]Radhakrishnan, K., "LSENS—A General Chemical Kinetics and Sensitivity Analysis Code for Homogeneous Gas-Phase Reactions. I. Theory and Numerical Solution Procedures," NASA RP-1328, Jan. 1994.

[21]Yee, H. C., "Construction of Explicit and Implicit Symmetric TVD Schemes and Their Applications," *Journal of Computational Physics*, Vol. 68, 1987, pp. 151–179.

[22]Yungster, S., "Numerical Simulation of Shock-Induced Combustion for Application to the Ram Accelerator Concept," Ph.D. Dissertation, Dept. of Aeronautics and Astronautics, Univ. of Washington, Seattle, WA, 1989.

[23]Yungster, S., Eberhardt, S., and Bruckner, A. P., "Numerical Simulation of Hypervelocity Projectiles in Detonable Gases," *AIAA Journal*, Vol. 29, No. 2, 1991, pp. 187–199.

[24]Cooper, K., "NPARC 2.0—Features and Capabilities," AIAA Paper 95-2609, July 1995.

[25]Young, V. Y., and Yee, H. C., "Numerical Simulation of Shock Wave Diffraction by TVD Schemes," AIAA Paper 87-0112, 1987.

[26]Yee, H. C., "Upwind and Symmetric Shock-Capturing Schemes," NASA TM-89464, Jan. 1987.

[27]Lehr, H. F., "Experiments on Shock-Induced Combustion," *Acta Astronautica*, Vol. 17, Nos. 4, 5, 1972, pp. 589–596.

[28]Matsuo, A., Fujiwara, T., and Fuji, K., "Flow Features of Shock-Induced Combustion Around Projectile Traveling at Hypervelocities," AIAA Paper 93-0451, Jan. 1993.

[29]Baldwin, B., and Lomax, H., "Thin Layer Approximation and Algebraic Model for Separated Turbulent Flows," AIAA Paper 78-257, Jan. 1978.

[30]Anderson, J. D., Jr., *Hypersonic and High Temperature Gas Dynamics*, McGraw–Hill, New York, 1989, p. 281.

Color reproductions courtesy of Ohio Aerospace Institute and NYMA, Inc.